Interplanetary Hydrogen Properties Observed from Mars

M. Mayyasi[1], E. Quémerais[2], D. Koutroumpa[2], I. Baliukin[3], A. Titova[3], V. Izmodenov[3], J. Clarke[4], J. Deighan[5], N. Schneider[5], S. Curry[6]

1 Center for Space Physics, Boston University, Boston, MA, USA
2 LATMOS-OVSQ, Université Versailles Saint-Quentin, Guyancourt, France
3 Space Research Institute (IKI) of Russian Academy of Sciences, Russia
4 Astronomy Department, Boston University, Boston, MA, USA
5 Laboratory for Atmospheric and Space Physics, University of Colorado Boulder, Boulder, CO, USA
6 Space Sciences Laboratory, University of California, Berkeley, California, USA

Journal: JGR
Keywords: IPH, Heliosphere, UV, Spectrograph, Mars, MAVEN

Abstract

Observations of the Lyman-α emissions from Interplanetary Hydrogen (IPH) atoms are made from Mars' orbit using a high spectral resolution instrument in echelle configuration. The measurements can uniquely be used to resolve IPH from planetary H emissions and to subsequently determine the brightness, velocity, and thermal broadening of the IPH flow along the instrument line of sight. Planned as well as serendipitous observations, both upwind and downwind of the flow, are analyzed to determine these IPH properties and to examine the variability of IPH brightness with solar activity through the declining phase of Solar Cycle 24. A heliospheric interface model was used to simulate and interpret the derived IPH properties. The results show that the IPH brightness trends with solar irradiance, the flow is fainter downwind than upwind, the IPH brightness is variable and non-negligible compared with planetary emissions, and that deriving thermal properties of IPH requires higher spectral resolution than is presently available. These results can improve the theoretical understanding of solar system dynamics by providing empirical constraints to simulations from the inner boundary of the heliosphere and can guide the development of future interplanetary missions.

Background

The motion of the solar system through the local interstellar medium (LISM) carves out a cavity around the Sun known as the heliosphere. Neutral H atoms populate the heliosphere, and these atoms originate from the solar wind, the interstellar medium, as well as from processes that neutralize protons via charge exchange throughout the region [Bertaux and Blamont, 1971; Lallement et al., 1993; Thomas and Krassa, 1971; Quémerais et al., 2006 and references therein]. The collective flow of these neutral H atoms through the solar system is called Interplanetary Hydrogen (IPH).

H atoms resonantly scatter Lyman-α photons. IPH properties have therefore been examined using Lyman-α emissions observed by multiple spacecraft from various points in the solar system [e.g., Baliukin et al., 2022; Galli et al., 2022; Zank et al. 2022]. It is found that the IPH flow direction emanates from the heliospheric 'nose' at $8.9 \pm 0.5^\circ$ ecliptic latitude and $252 \pm 0.7^\circ$ ecliptic longitude [Lallement et al., 2005; 2010]. The IPH velocity ranges between 18 ± 2 km/s and 25.7 ± 2 km/s, and varies with solar activity, line of sight, and distance from the Sun [Vincent et al., 2011; Koutroumpa et al., 2017]. The abundance, velocity, and thermal distribution of these atoms can vary over solar cycle timescales and can be used to determine how the Sun and the LISM interact [e.g., Katushkina et al. 2019].

The effects of the Sun on the flow, such as radiation pressure are strongest near the Sun and fall off as the square of the distance such that within a few AUs from the Sun, the solar wind ionizing power creates a void of neutral H atoms [Quémerais et al., 2014]. In this work, seven years of observations obtained from ~1.6 AU (Mars' orbit at its aphelion) were examined to derive IPH properties over the relatively moderate maximum through minimum of Solar Cycle 24. Observations from the upwind flow direction as well as downwind to the flow were analyzed and compared. A model simulating the heliospheric interface was used for comparison [Izmodenov and Alexashov, 2015; 2020]. The results from this analysis can empirically constrain IPH models at 1.6 AU, where few IPH measurements have been made, and can refine our understanding of how the solar system interacts with the LISM in the dynamic heliosphere [e.g., Izmodenov, 2007, Vincent et al., 2014].

Observations

The Mars Atmosphere and Volatile Evolution (MAVEN) spacecraft has been in orbit since September 2014, carrying an instrument suite that includes an Imaging Ultraviolet Spectrograph (IUVS) with a high-spectral resolution echelle component [McClintock et al., 2014; Jakosky et al., 2105; Mayyasi et al., 2022a]. The high spectral-resolution capabilities were designed to resolve hydrogen and deuterium (D) Lyman-α emissions at 121.567 and 121.534 nm, respectively [e.g., Mayyasi et al., 2017a; 2019a]. This optical design can also resolve planetary H from IPH Lyman-α emissions at times

when there is sufficient Doppler shift between the two H populations along the instrument line of sight.

Once a spectrally resolved IPH emission spectrum is obtained, the data can be used to derive brightness, velocity, and thermal broadening of the IPH flow along the line of sight [Mayyasi et al., 2017b]. Since both upwind and downwind observations are available, an additional useful diagnostic to derive is the variability in upwind to downwind properties of the IPH flow using observations made close in time. This diagnostic would be useful for interpreting IPH flow dynamics in the inner heliosphere [Clarke et al., 1998]. A unique feature of this dataset is the availability of both upwind as well as downwind IPH observations obtained in the same epoch.

The MAVEN IUVS instrument makes routine observations of IPH to calibrate the spectrograph as well as to monitor for possible signs of degradation in the instrument [Mayyasi et al., 2017b]. During a few months in each Mars Year (MY), typically around aphelion when the Solar longitude (Ls) is less than 180°, the velocity of Mars along its orbit (~24 km/s) produces a maximum Doppler shift with the IPH flow, as shown in **Figure 1**. The upwind IPH direction is at RA and DEC of 16.9^h and -15.5°, respectively. The downwind IPH direction is at an RA and DEC of 4.9^h and -15.5°, respectively. The crosswind IPH direction is at an RA and DEC of 10.9^h and 0°, respectively. We adopt an average IPH velocity of ~23.3 km/s relative to the Sun, resulting in a maximum blue-ward Doppler shift of ~46 km/s at ~78° Ls when looking upwind to the IPH flow from Mars and a maximum red-ward Doppler shift of ~39 km/s near Ls ~73° looking downwind.

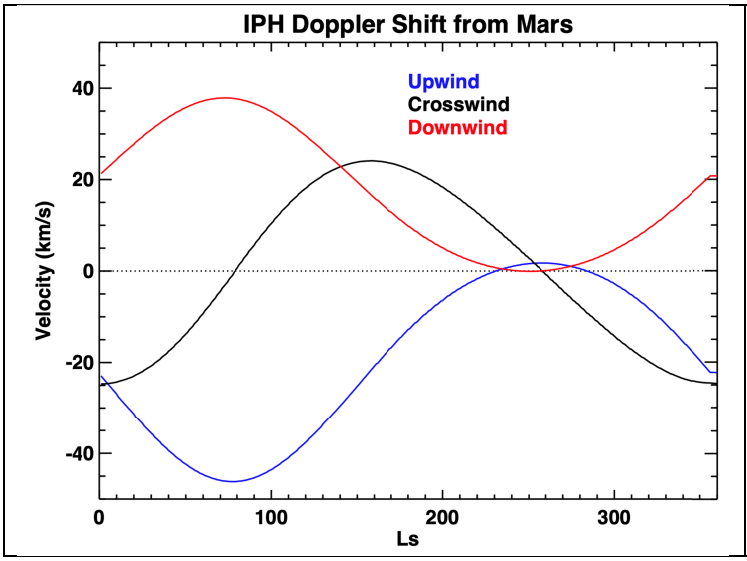

Figure 1. The Doppler shift of the IPH flow along the line of sight from Mars as a function of the planet's orbital location, denoted by solar longitude (Ls). Looking upwind (blue), crosswind (black), and downwind (red) to the IPH flow results in a variable Doppler shift throughout Mars' orbital path. A horizontal dotted black line is shown at 0 km/s for reference.

The IUVS/ECH line spread function has a full-width-half-max (FWHM) of ~17.5 km/s. Therefore, a filter of at least 2×FWHM (~35 km/s) was considered optimal for detecting and analyzing IPH properties in the IUVS/ECH limb scans. These detections do not overlap with planetary D Lyman-α emissions, that are separated from the Mars at-

rest H wavelength by over 6×FWHM. Due to this criterion, observations where the line of sight was crosswind to the IPH flow had Doppler shifts (peaking at ±25 km/s) that are too small to spectrally resolve the IPH feature and are therefore not analyzed in this work.

During the optimally Doppler shifted upwind conditions, MAVEN conducted planned IPH observing campaigns. In Dec 2019, interstellar Comet 2I/Borisov was making its closest approach at a time when MAVEN/IUVS had favorable viewing geometry. The line of sight to the comet serendipitously captured an optimally Doppler shifted downwind IPH flow. Moreover, nominal science observations have been found to fortuitously have a resolvable IPH component when the instrument line of sight is pointed off the planetary disk and through the limb. The observations that are relevant to this work, relative to the available archive of observations, are highlighted in **Figure 2**.

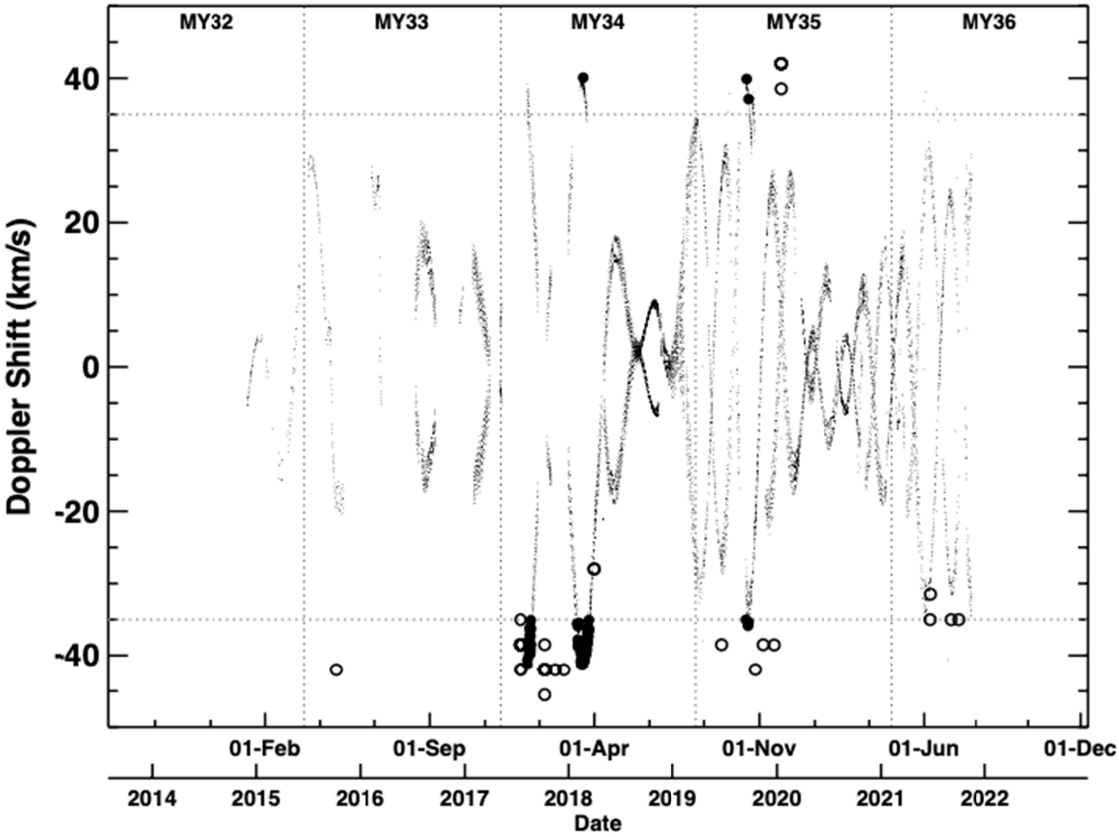

Figure 2. MAVEN IUVS timeline of Doppler shift from all limb-scans (dots) and dedicated IPH campaign (open circles). Horizontal black dotted lines denote the spectral resolvability limit for IPH emissions at ±35 km/s. An additional 90 data points (solid circles) are available from fortuitous limb pointing that include upwind (<-35 km/s) as well as downwind (>35 km/s) IPH emissions suitable for analysis.

Between Nov 2014 and Nov 2021, a total of 125 observations were found to be suitable for resolving the IPH emission to derive the properties of the flow. Of these useable observations, 37 are obtained from dedicated IPH campaigns, and 88 are from

limb scans. Of the dedicated IPH campaign data points, 33 were made upwind of the IPH flow, and 4 were made downwind. Of the 88 limb scans, 85 were upwind and 3 were downwind of the IPH flow.

The IUVS/ECH data, obtained from both the dedicated IPH campaigns as well as limb scan observations have multiple frames (images) per orbit, ranging between 20-60. A single frame consists of a 29 second exposure for limb scans, and 60 second exposures for campaign observations. For all the observations used here, the IPH flow direction does not vary significantly from frame to frame within a single orbit. Therefore, frames from each orbit are averaged to produce a single spectrum for that orbit to optimize the signal to noise ratio [e.g., Mayyasi et al., 2022a].

Method

The MAVEN spacecraft orbits within the extended Mars H corona. Therefore, all Lyman-α observations made along the IUVS/ECH line of sight include a planetary H emission component. A sample spectrum including Mars H, Mars D, and IPH emissions and their best fits is shown in **Figure 3**.

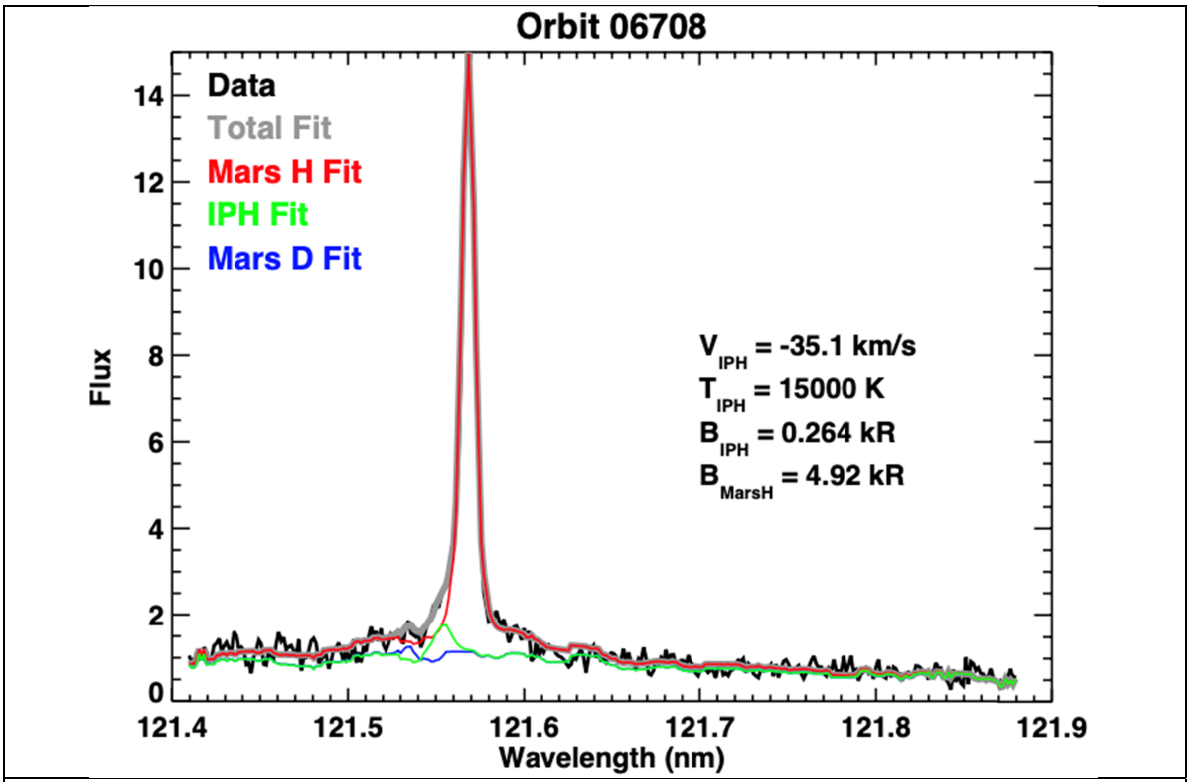

Figure 3. Sample MVN/IUVS/ECH limb scan with planetary H and D as well as IPH Lyman-α emissions from orbit 6708, taken on March 12, 2018, when Mars was at 142° Ls. The MAVEN spacecraft was 1.56 AU from the Sun and 3141 km above the surface of Mars. The instrument line of sight was pointed at 261.6° ecliptic longitude and -0.05° ecliptic latitude. The averaged spectrum (black) is used to iteratively obtain the best fits for the

Mars H (red), IPH (green), and Mars D (blue) emissions. The total best fit curve (grey) sums the three emissions as well as the detector background level. The relevant IPH properties derived from this observation are listed on the right legend. V represents velocity, T represents temperature, and B represents brightness.

To resolve each emission and derive the IPH properties, minimum variance analysis was used. First estimates of the (1) planetary at-rest H emission peak wavelength, (2) Doppler shifted IPH emission peak wavelength, (3) thermal broadening of the IPH emission, (4) percentage of thermal H contribution to the total Lyman-α emission, and (5) percentage of IPH contribution to the total Lyman-α emission are derived from the spacecraft ephemeris and literature adopted values. An iterative algorithm was then run that varied the first estimates within set ranges and generates a spectrum for each combination of the five parameters. The modeled spectrum was compared with the data and a matrix of χ^2 values was generated for each combination of the parameters. The parameter set that produced the minimum χ^2 value was used to generate the best-fit curve, as shown in **Fig. 3**. The resulting best fit curve for each of the 125 spectra was examined by eye to confirm accurate representation of the data.

The first estimate for at-rest emission peak wavelength for Mars H is 121.567 nm. The first estimate for emission peak wavelength of IPH was derived from the line of sight geometry that accounted for the velocity of Mars, MAVEN, and the IPH flow along the instrument line of sight. The range of velocities for each emission peak used in the fitting algorithm were $\pm$0.2$\times$FWHM of their first estimates, varied in 0.1$\times$FWHM increments, to account for minimal velocity changes due to the motion of the MAVEN spacecraft around Mars (~2.5 km/s) as well as for the IUVS/ECH spectral resolution (~3.5 km/s/binned pixel [Mayyasi et al., 2017b]).

Mars H atoms are typically thermalized at ~200-350 K [Mayyasi et al., 2022b]. These temperatures do not significantly broaden the planetary emission line profile beyond a characteristic shape, empirically determined by the instrument line spread function (LSF) [Mayyasi et al., 2022a]. IPH atoms are typically several thousands of degrees K, resulting in a thermally broadened Lyman-α emission profile [Wu and Judge, 1980; Bertaux et al., 1985; Clarke et al., 1998; Mayyasi et al., 2017b]. An optimal line shape to use for IPH emission line profile fits was obtained by convolving the instrument LSF with a Voigt profile of some temperature (LSF$\otimes$Voigt). The IPH temperature range considered here was between 11,000 K and 15,000 K, varied in 500 K increments.

The smaller the Doppler shift of the IPH flow along the instrument line of sight, the closer the overlap between Mars H and IPH emissions. The flux value of the Mars H peak emission and that of the IPH emission, at the assumed Doppler shift were used as first estimates to constrain the fits of the emission line shapes generated by the fitting algorithm. These peak fluxes were then varied by $\pm$10% in 2% increments in the iterations to obtain an optimal fit to the data.

Using this methodology, the best fit spectra generated for IPH and Mars H emissions were integrated across wavelength to derive brightness [e.g., Mayyasi et al., 2022a]. The IPH temperature and velocity, along the line of sight, were obtained from the remaining best fit parameters directly.

Results

The distribution of the observations relative to the IPH upwind and downwind directions is shown in **Figure 4**. The IPH upwind direction is at ecliptic longitude and latitude of 252° and 7.4°, respectively. The downwind direction is at ecliptic longitude and latitude of 7.39° and -7.5°, respectively. The IPH upwind campaign observations deviated from the upwind flow direction by anywhere from ~3° to 60°, with an average of ~14°. The upwind limb scan observations deviated between ~11° to 53° from the upwind flow direction, with an average of ~30°. The IPH downwind campaign observations deviated by anywhere between ~37° to 46° of the downwind flow direction, with an average of ~42°. The downwind limb scan observations deviated between ~25° to 30° from the downwind flow direction, with an average of ~28°.

Figure 4: The distribution of observations relative to the upwind and downwind directions of the IPH flow, in ecliptic coordinates. Blue data points represent upwind observations made from IPH campaigns (open circles) and from limb scans (dots). Red data points represent downwind observations with similar symbols as used for upwind. The IPH upwind flow direction is shown as a black cross and the downwind direction is shown as a grey cross.

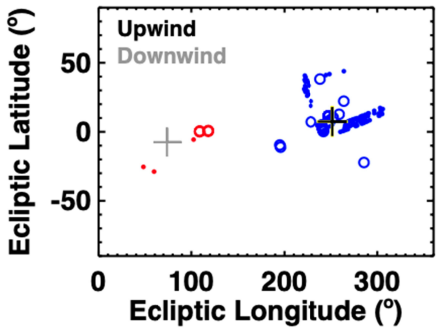

To date, observation of IPH properties from Mars' orbital location have been limited [e.g., Mayyasi et al., 2017b]. On the other hand, observation of IPH properties from Earth's vicinity are relatively abundant [e.g., Galli et al., 2022]. Such observations from each planet would serve as useful constraints to inner heliospheric models of the IPH flow and its variability. The orbital distribution of the observations relative to the Sun and Earth are shown as a function of angle from upwind IPH flow in **Figure 5**.

The observations were predominantly made during aphelion when the relative Doppler from Mars was greatest. For upwind observations, the IPH campaign data points varied between 1.53 and 1.67 AU, with an average of 1.64 AU. For the upwind limb scans, the observations ranged between 1.56 and 1.66 AU with an average of 1.59 AU. For the downwind observations, the IPH campaign data points were at ~1.57 AU. The downwind limb scans ranged between 1.58 and 1.67 AU with an average of 1.64 AU.

In the observations analyzed here, the Earth-Mars distance spanned 1.11-2.65 AU for upwind IPH campaign observations, with an average at 2.44 AU. The Earth-Mars distance for the limb-scan upwind data points ranged between 1.29-2.67 AU with an average of 1.72 AU. The downwind IPH campaign observations were all made at an Earth-Mars distance of 2.08 AU, and the downwind limb scan observations were at an Earth-Mars distance that ranged between 1.48 and 2.66 AU with an average of 2.26 AU.

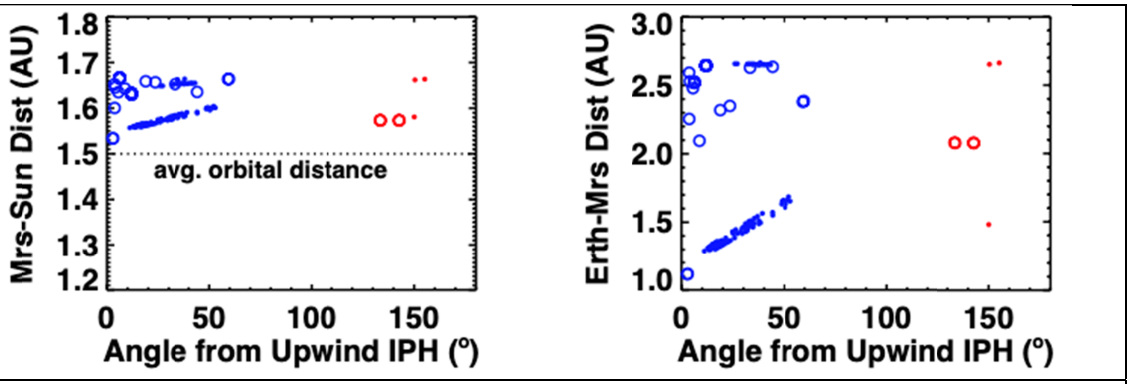

Figure 5. Orbital distance of the observations made at Mars relative to the Sun (Left) and to Earth (Right). Open circles are from IPH campaigns, small solid circles are from limb-scans. Blue data points correspond to upwind-oriented observations and red data points correspond to downwind-oriented observations.

The IPH properties derived from the fitting algorithms are shown in **Figure 6**, as a function of angle from the upwind IPH flow. The IPH emission brightness was obtained by integrating the best fit emission line curve across wavelengths. The uncertainty in each co-added spectrum was derived by examining a background region of the detector away from the emission region as described in [Mayyasi et al., 2017b; 2022a]. The resulting IPH brightness from upwind observing campaigns varied between 0.407 and 0.575 kR with an average of 0.478 kR. The IPH brightness in the upwind limb-oriented observations ranged between 0.254 and 0.656 kR with an average of 0.367 kR. The best fit IPH brightness in the downwind IPH campaign data rangef between 0.266 and 0.354 kR with an average of 0.306 kR. The best fit IP brightness for the downwind oriented limb data ranged between 0.319 and 0.424 kR with an average of 0.365 kR. The uncertainties in the spectra varied for each data point, and ranged between 0.020 and 0.070 kR, with an average of 0.040 kR. Relative to the IPH emission, the uncertainties ranged between 4% and 26% with an average of 11%.

The IPH velocity is presented both as Doppler shift along the line of sight, in km/s, as well as in wavelength, relative to the at-rest Lyman-α line center. For upwind IPH campaign observations, the Doppler shift varied between -28.0 (-0.011) and -45.5 (-0.018) km/s (nm), with an average of -38.8 (-0.016) km/s (nm). For upwind limb scans, the Doppler shift varied between -35.0 (-0.014), as constrained for visibility, and -41.2 (-0.017) km/s (nm) with an average of -38.5 (-0.016) km/s (nm). For downwind IPH campaign observations, the Doppler shift varied between 38.5 (0.016) and 42.0 (0.017)

km/s (nm) with an average of 41.2 (0.017) km/s (nm). For the downwind oriented limb scans, the Doppler shift varied between 37.1 (0.015) and 40.1 (0.016) km/s (nm) with an average of 39.0 (0.016) km/s (nm). These results are consistent with the first estimate predictions of Doppler shift derived from the line of sight observing geometry.

The best-fit temperature of the IPH flow covered the full range of fitting values. For upwind IPH campaign observations, the fit temperatures averaged ~14,100 K while the upwind limb scans averaged ~14,400 K. The downwind IPH campaign observation best fit temperatures averaged of ~11,800 K while the downwind limb scans averaged ~12,000 K.

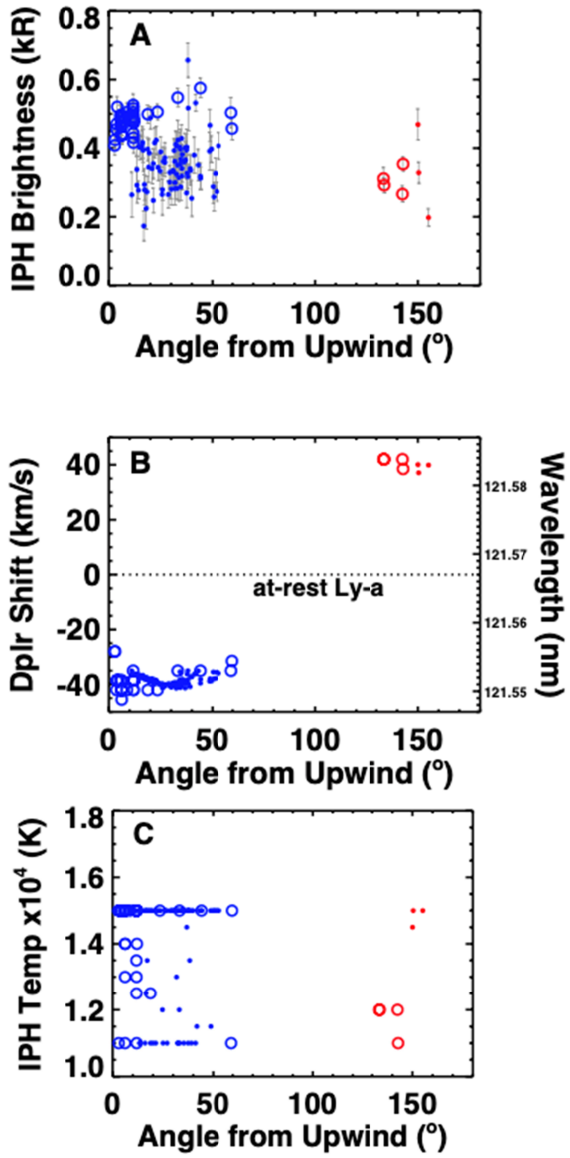

Figure 6. (A) The derived IPH brightness in kR, (B) Doppler shift in km/s and wavelength in nm, and (C) best-fit temperature in 10,000s K as a function of angle from the upwind IPH flow. The dashed line in panel (B) represents the at-rest Lyman-α Doppler shift (wavelength) of 0 km/s (121.567 nm). Unfilled circles represent properties derived from IPH campaigns. Smaller dots correspond to properties derived from limb scans. Blue symbols represent observations made upwind of the IPH flow and red symbols represent observations made downwind of the IPH flow.

The best fit Mars H emissions were integrated across wavelength to derive a planetary H brightness that is shown in **Figure 7**. Martian H atoms are generally thermalized within the collisional region of the upper atmosphere [Matta, 2013;

Mayyasi et al., 2018; 2019b]. During IPH campaigns, the line of sight was oriented tangentially to Mars or away from the planet, and so, the Mars H brightness was expected to be fainter than when the line of sight was directed toward the planet. The average Mars H brightness was verified to be lower during IPH campaigns and ranged between 0.198 kR and 3.00 kR with an average of 1.01 kR. In the limb-oriented observations, the Mars H brightness values were larger and ranged between 0.417 kR and 5.00 kR with an average of 3.57 kR.

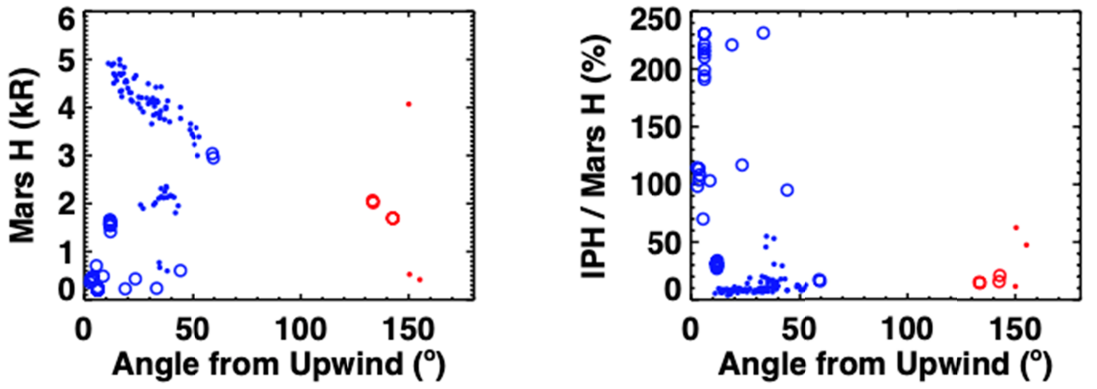

Figure 7. (Left) The best fit brightness of the thermal martian H emissions as a function of IPH upwind flow angle. (Right) The percentage of IPH to Mars H brightness. Open circles indicate data observed during IPH campaigns. Dots indicate data obtained during limb scan observations. Blue data points indicate upwind observations. Red data points are obtained pointing downwind of the IPH flow.

Relative to the Mars H emission brightness, the IPH brightness can range between a significant or negligible component. For IPH campaign observations, the line of sight was optimized to capture IPH emissions, that can often exceed those from planetary H atoms and dominate the total Lyman-α spectral emission. Upwind IPH campaign observations showed the IPH contribution to vary between 15% and 231% with an average of 111%. The upwind limb observations showed the IPH contribution to vary between 8% and 55% with an average of 18%. In the downwind IPH campaign observations, the IPH contribution varied between 14% and 21% with an average of 17%. In the downwind limb scans, the IPH contribution ranged between 7% and 10% with an average of 9%.

To validate the results, a comparison of Mars H and IPH emission brightness was made over a range of solar illumination conditions along the line of sight, as shown in **Figure 8**. Variability in planetary H emissions is a consequence of multiple factors that include season, atmospheric dynamics, and observational geometry. The variation in brightness with illumination, denoted by solar zenith angle (SZA), of the tangent point to Mars along the line of sight demonstrated these effects. As expected, the Martian H brightness decreased with SZA [Mayyasi et al., 2022b], while the IPH brightness did not show similar trends with SZA.

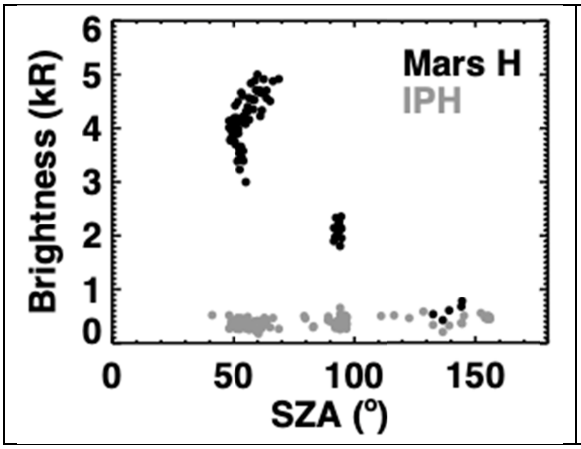

Figure 8. The variability of H emission brightness with solar illumination, denoted by solar zenith angle. The black dots show the variation in Mars thermal H emissions that decrease notably with increasing SZA. Grey dots show the near-constant IPH brightness with SZA.

The MAVEN/ECH observations utilized here included one data point in Mars Year (MY) 33, 107 data points in MY34, 13 datapoints in MY35, and 4 data points in MY36. During this timeline, solar activity was declining through Solar Cycle 24 into its minimum phase (~mid Sep 2019) through the rising activity phase of Solar Cycle 25. The Solar Lyman-α irradiance, averaged over a solar rotation cycle (28 days), was derived from terrestrial measurements, and shown for reference in **Figure 9** [Machol et al., 2019].

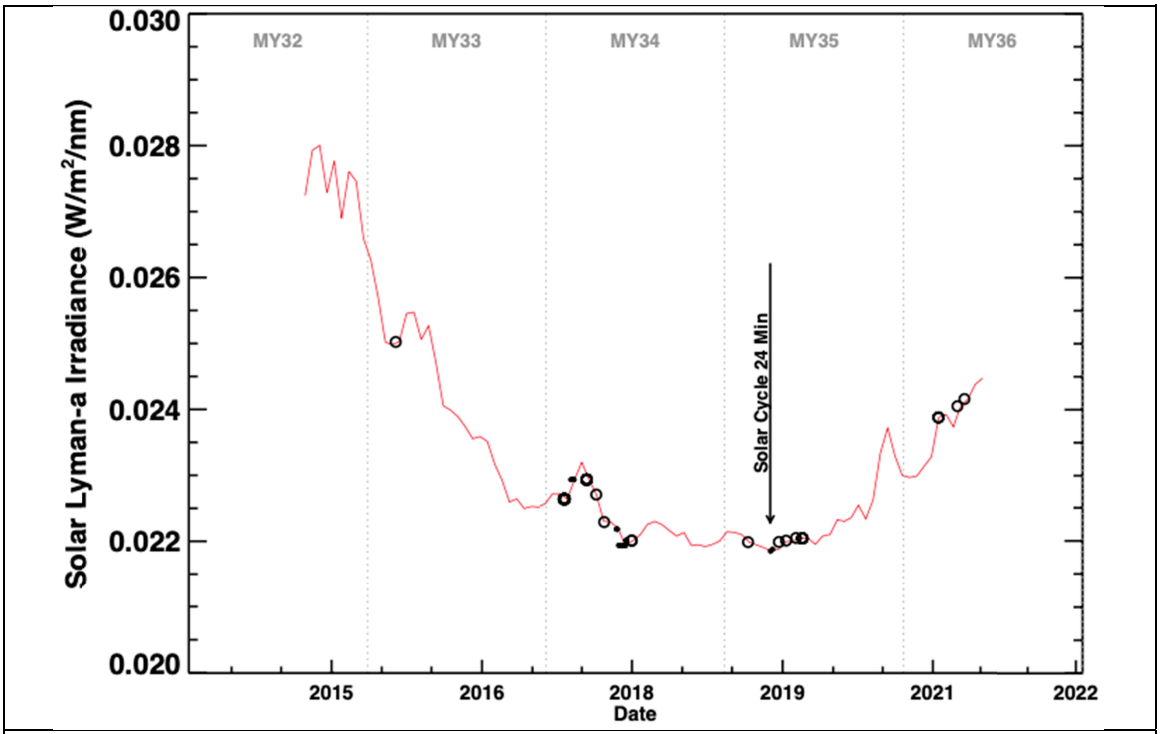

Figure 9. Sampling of IPH observations with time and solar activity, across the MAVEN mission timeline. The red line shows the 28-day averaged Solar Lyman-α irradiance with symbols indicating the times of the IPH observations analyzed in this work. Black open circles indicate IPH campaign observations and small black circles indicate limb pointed observations. Vertical grey dotted lines separate MYs. An arrow indicates the

minimum solar irradiance measurements, indicating the minimum activity period of Solar Cycle 24 (mid-Sep 2019).

To determine the effects of solar activity on the derived IPH brightness, the Solar Irradiance was scaled to the MY33 single data point, as shown in **Figure 10**. The IPH brightness followed the general trend of solar activity brightness with some scatter about the irradiance trendline. The IPH brightness was 0.506 kR for the single datapoint in MY33, and averaged 0.381 kR in MY34, 0.363 kR in MY35, and 0.520 kR in MY36, for data from each MY (from combined upwind, downwind, IPH campaign and limb-oriented data). The Solar Irradiance averaged 0.0240 W/m^2/nm in MY 33, 0.0220 W/m^2/nm in MY 34, 0.0220 W/m^2/nm in MY35, and 0.0237 W/m^2/nm in MY 36.

The dataset includes a unique feature of having both upwind and downwind observations for IPH obtained around the same epoch in MY35, during Solar Cycle 24's minimum phase. Of the 13 observations available from that epoch, 7 were upwind and 6 were downwind. Four of the seven upwind observations were obtained during IPH campaigns, and three were obtained during limb-pointed scans. Additionally, four of the six downwind observations were obtained during IPH campaigns, and two were obtained during limb-pointed scans. To compare the upwind and downwind IPH properties, an adjustment to the data was implemented to normalize the effects of solar activity.

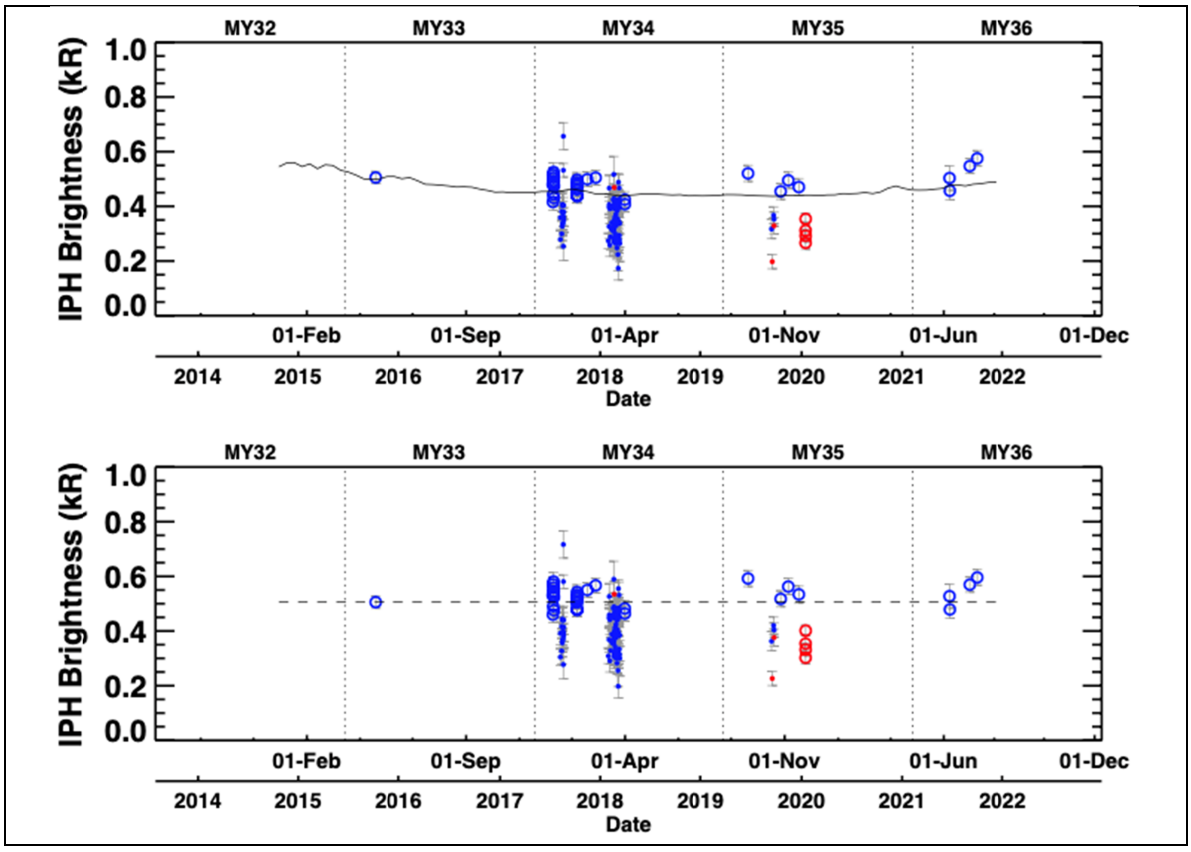

Figure 10. IPH brightness measurements with time. (Top) The black line indicates the scaled solar Lyman-α irradiance, measured from Earth, averaged over 28 days to account for solar rotation variations. (Bottom) Same as Top but with the solar irradiance normalized (dashed black line) and with it the brightness values to account for solar activity variations across the mission timeline.

Solar irradiance variability was accounted for by constraining the brightness values to the irradiance in MY33 (at 0.025 W/m^2/nm) and normalizing the Solar irradiance for remaining data points to that value by adjusting the IPH brightness by a similar scaling factor as the irradiance normalization factor. This correction is shown in **Fig. 10B**. The normalized IPH brightness in MY33 remained unchanged and the averages for subsequent data points were 0.427 kR in MY34, 0.414 kR in MY35, and 0.543 kR in MY36.

Using the irradiance-normalized values, the average brightness, temperature, and Doppler shift of all upwind IPH observations from MY35 (campaign and limb-pointed) were 0.484 kR, 15000 K, and -37.7 km/s, respectively. The average brightness, temperature, and Doppler shift of all downwind observation from MY35 (campaign and limb-pointed) are 0.332 kR, 12800 K, and 40 km/s.

Interpretation

The IPH brightness showed that downwind H populations were fainter than the upwind populations. This was expected, as H atoms are more depleted closer to the Sun due to photoionization and charge exchange that subsequently diminish their collective Lyman-α emissions. These empirical results were consistent with previous findings [Clarke et al., 1995; 1998]. When normalized to account for solar cycle variability, the values of solar irradiance and IPH brightness, averaged for each MY, correlated well (0.98 correlation coefficient) as would be causally expected for observations resulting from solar resonant scattering photons along a nearly constant column of IPH atoms.

The IPH velocity showed a decreasing trend as the line of sight moved away from up/downstream orientation toward cross-stream orientation, as was expected. The velocity scatter for similar viewing angle was due to the velocity of the MAVEN spacecraft. In the next section the velocity derived relative to the solar rest frame demonstrates a smoother trend, as expected.

The IPH temperature derivations were constrained to a range of values that are consistent with previous models and observations of IPH temperatures in the inner heliosphere [Costa et al., 1999; Quémerais et al., 2006]. However, the best fits showed that the temperature range may have limited the fitting algorithm. A broader range of temperatures was applied, spanning 10,000 – 28,000 K, and showed the scatter in the best-fit temperatures to persist and to have minimal consequences on the brightness derivations that integrate across the spectral range. The absence of a smoother

temperature trend is likely due to the data fitting algorithm that would result in very small changes in the χ^2 value for temperatures that are a few thousand K different paired with the limited spectral resolution of the data. Due to these factors, the derived temperatures should not be considered definitive.

In examining the relative contribution of IPH to the planetary emission from Mars' orbit, it was found that the IPH contribution ranged between significant (close to upwind orientations) and comparable (close to downwind orientation). This result is critical for lower-resolution Lyman-α observations made from Mars (and other planetary bodies with thermal H emissions) where assumptions are made to ignore IPH contributions or to assume a fixed value across a range of observing conditions.

Comparison to Model

IPH observations made in the inner heliosphere and relatively close to the Sun can serve to constrain heliospheric models due to the unique differences of flow properties along the various lines of sight in the region where photoionization, charge exchange with solar wind, solar gravity, and radiation pressure are dynamically affecting neutral H atoms. Additionally, the properties of interplanetary H atoms can be compared with models and observations of interplanetary He atoms for insights into the differences in flow dynamics throughout the heliosphere [e.g., Bzowski et al., 2019].

A heliospheric simulation tool was used to independently determine the brightness, Doppler shift, and temperature values of IPH atoms for the observations utilized here. The simulation used a 3-dimensional time-dependent kinetic-magnetohydrodynamic model that accounted for multi-constituent solar wind and interstellar plasmas, solar and interstellar magnetic fields, different interstellar hydrogen atom populations, and the latitudinal dependence of solar wind [Izmodenov and Alexashov, 2015; 2020]. This global heliospheric model calculated the H distribution at a sphere of radius 70 AU from the Sun as the boundary condition for a local model [Izmodenov et al. 2013, Katushkina et al. 2015].

The local model simulated the H distribution inside the 70-AU sphere by solving the kinetic equation to account for non-Maxwellian kinetic features, temporal variations of solar radiation pressure, and ionization rates during the solar cycle. Charge exchange ionization rates were taken from the analysis of the SOHO/SWAN Lyman-α observations [Katushkina et al., 2019; Koutroumpa et al., 2019] that were normalized using in situ data from the OMNIWeb database collected in the ecliptic plane (https://omniweb.gsfc.nasa.gov/). The dependence of radiation pressure on time, radial velocity, and heliolatitude of H atoms was adopted from Kowalska-Leszczynska et al. [2020]. The total solar Lyman-α flux measured at the Earth's orbit was taken from Machol et al. [2019] (http://lasp.colorado.edu/lisird/data/composite_lyman_alpha/).

Using the H distribution from the model simulations, the solar Lyman-α radiation backscattered by H atoms was calculated. Single-scattered photon emissions were calculated by integrating the radiative transfer equation, and the multiple scattering emissions were calculated using the radiative transfer code developed by Quémerais [2000], which utilized the Monte Carlo method. In the simulations done for this work, the spectral properties that are moments of the Lyman-α spectrum were calculated. Namely, the brightness, line shift (Doppler shift), and line width (temperature) were obtained for the 125 observations made by MAVEN/IUVS.

The model brightness, Doppler shift, and temperature values were compared with the values derived from the observations, as shown in **Figure 11**. The simulated brightness values were consistently higher than the observed brightness values by a factor of two for both upwind and downwind datapoints. The comparison was therefore shown between the data and the modified simulated values (that were scaled by 0.5). This discrepancy may be in part due to differences between the model and data calibration methods [Mayyasi et al., 2017b; 2022a; Baliukinet al., 2022]. At the time of this writing, upcoming HST/STIS observations of the upwind IPH are planned to occur simultaneously with MAVEN/IUVS observations (HST GO-Cycle 17196). Subsequent analysis of these data would help address any potential data/model calibration offsets.

The Doppler shifts, converted into the solar rest frame (SRF) were compared for the empirical and simulated results. These are found to be in good agreement for both upwind and downwind observations.

The simulated temperatures were, on average, ~20% cooler and showed less scatter than the average temperatures derived from the fits to the data. The model predicts higher temperatures for downwind IPH atoms than for upwind atoms, as is consistent with previous observations [Izmodenov, 2006; Katushkina and Izmodenov, 2011].

In summary, IPH atoms observed from Mars' vantage have provided constraints that show some agreements as well as disagreements with theoretical predictions. Understanding these differences will refine our understanding of how the IPH flow is affected by interface dynamics at the outer edge of the heliosphere as the flow propagates closer to the Sun. These and future analyses can further elucidate how solar drivers affect heliospheric dynamics in the inner solar system.

Data Availability Statement

The MAVEN limb data used in this study are available on the NASA PDS Atmospheres Node at: https://pds-atmospheres.nmsu.edu/data_and_services/atmospheres_data/MAVEN/maven_main.html. IUVS echelle level1a data were used and reduced using the most up-to-date pipeline [Mayyasi et al., 2022a].

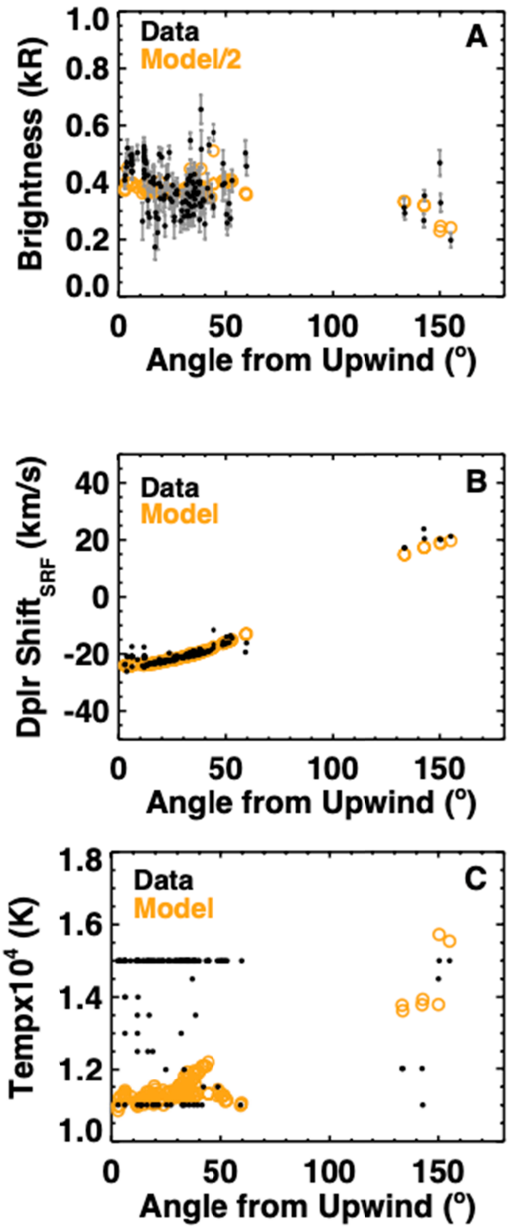

Figure 11. Data-model comparisons. Observations are shown as black dots and model values are show as yellow circles for all IPH data analyzed here (campaign and limb scans). Upwind observations are at angles less than 70° from upwind. Downwind observations are at angles larger than 130°. In panel (A) the observed brightness and its uncertainty (grey error bars) are compared to simulated values that have been scaled by a factor of 0.5. In panel (B), the Doppler shifts of observed and simulated values are shown in the solar rest frame (SRF). Panel (C) shows the temperatures obtained by the fits to the data as well as the model predictions.

Acknowledgements

This work was funded, in part, by NASA contract #1000320450 from the University of Colorado to Boston University. MM acknowledges the MAVEN mission for supporting the analysis of IUVS data. The MAVEN mission is supported by NASA in association with the University of Colorado and NASA's Goddard Space Flight Center.

References

Baliukin I. I., Bertaux J.-L., Bzowski M., Izmodenov V. V., Lallement R., Provornikova E., Quémerais E. (2022), Backscattered solar Lyman-α emission as a tool for the heliospheric boundary exploration», Space Science Reviews, 218, 45, DOI: 10.1007/s11214-022-00913-3

Bertaux, J. L., and J. E. Blamont (1971), Evidence for a source of an extraterrestrial hydrogen Lyman-alpha emission, Astron. Astrophys., 11, 200–217.

Bertaux, J. L., R. Lallement, V. Kurt, E. Mironova (1985), Characteristics of the Local Interstellar Hydrogen determined from PROGNOZ 5 and 6 interplanetary Lyman α line profile measurements with a hydrogen absorption cell, Astron. Astrophys., 150, 1 – 20, 1985A&A…150….1B.

Bzowski, M., A. Czechowski, P. Frisch, S. Fuselier, A. Galli, J. Grygorczuk, J. Heerikhuisen, H. Kucharek, D. McComas, E. Möbius, N. Schwadron, J. Slavin , J. Sokół, P. Swaczyna, P. Wurz, and E. Zirnstein (2019), Interstellar Neutral Helium in the Heliosphere from IBEX Observations. VI. The He+ Density and the Ionization State in the Very Local Interstellar Matter, Ap. J., 882:60 (15pp), doi:10.3847/1538-4357/ab3462.

Clarke, J., R. Lallement, J-L. Bertaux, E. Quémerais, H. Scherer (1995), HST/GHRS Observations of the Interplanetary Medium Downwind and in the Inner Solar System, Ap. J., 448, 893 – 904, 1995ApJ…448..893C.

Clarke, J., R. Lallement, J-L. Bertaux, H. Fahr, E. Quémerais, H. Scherer (1998), HST/GHRS Observations of the Velocity Structure of Interplanetary Hydrogen, Ap. J., 499, 482 – 488.

Costa, J., R. Lallement, E. Quémerais, J.L. Bertaux, E. Kyrölä, W. Schmidt, Heliospheric interstellar H temperature from SOHO/SWAN H cell data. Astron. Astrophys. 349, 660–672 (1999)

Galli., A., I. Baliukin, M. Bzowski, V. Izmodenov, M. Kornbleuth, H. Kucharek, E. Möbius, M. Opher, D. Reisenfeld, N. Schwadron, P. Swaczyna (2022), The Heliosphere and Local Interstellar Medium from Neutral Atom Observations at Energies Below 10 keV, Sp. Sci. Rev., 218:31, https://doi.org/10.1007/s11214-022-00901-7.

Izmodenov V. V. (2006), in ‘V. Izmodenov and R. kallenbach (eds.) ISSI Scientific Report´ No. 5, p45-64, ESA-ESTEC, Paris, The Physics of the Heliospheric Boundaries.

Izmodenov V. V., Katushkina O. A., Quemerais E., Bzowski M. (2013), in ‘Quemerais E., Snow M., Bonnet R.-M., eds, ISSI Scientific Report´ Series, Vol. 13, Cross-Calibration of Far-UV Spectra of Solar system Objects and the Heliosphere. Springer-Verlag, New York, p. 7

Izmodenov, V. (2007), Filtration of Interstellar Atoms through the Heliospheric Interface, Sp. Sci. Rev., 130: 377–387, DOI:10.1007/s11214-007-9203-5.

Izmodenov, V. and D. Alexashov (2015), Three-dimensional Kinetic-MHD Model of the Global Heliosphere with the Heliopause-surface Fitting, Astrophys. J. Suppl. Series, Special Issue 2015, v 220, 2, doi:10.1088/0067-0049/220/2/32.

Izmodenov, V. V., D.B. Alexashov, Magnitude and direction of the local interstellar magnetic field inferred from Voyager 1 and 2 interstellar data and global heliospheric model. Astron. Astrophys. 633, L12 (2020). https://doi.org/10.1051/0004-6361/201937058

Jakosky, B. (2015), MAVEN explores the Martian upper atmosphere, Science, 360, 6261, doi:10.1126/science.aad3443.

Katushkina, O. A., V. V. Izmodenov (2011), Spectral Properties of the backscattered solar Ly-alpha radiation in the heliosphere: a theoretical search of the heliospheric boundaries effects, Ad. Space Res., doi:10.1016/j.asr.2011.08.026.

Katushkina, O. A., V. V. Izmodenov, D. B. Alexashov (2015), Direction of interstellar hydrogen flow in the heliosphere: theoretical modelling and comparison with SOHO/SWAN data, Monthly Notices of the Royal Astronomical Society, Volume 446, Issue 3, Pages 2929–2943, https://doi.org/10.1093/mnras/stu2218.

Katushkina, O., V. Izmodenov, D. Koutroumpa, E. Quémerais, L. Jian (2019), Unexpected Behavior of the Solar Wind Mass Flux During Solar Maxima: Two Peaks at Middle Heliolatitudes, Solar Phys., 294:17, https://doi.org/10.1007/s11207-018-1391-5.

Koutroumpa, D., E. Quémerais, O. Katushkina, R. Lallement, J.L. Bertaux, W. Schmidt, Stability of the interstellar hydrogen inflow longitude from 20 years of SOHO/SWAN observations. Astron. Astrophys. 598, A12 (2017). https://doi.org/10.1051/0004-6361/201629840

Kowalska-Leszczynska, I., M. Bzowski, M.A. Kubiak, J.M. Sokół, Update of the solar Lyα profile line model. Astrophys. J. Suppl. Ser. 247(2), 62 (2020). https://doi.org/10.3847/1538-4365/ab7b77.

Lallement, R., J. L. Bertaux, and J. T. Clarke (1993), Deceleration of interstellar hydrogen at the heliospheric interface, Science, 260(5111), 1095.

Lallement R., E. Quémerais, J.L. Bertaux, S. Ferron, D. Koutroumpa, R. Pellinen, Deflection of the interstellar neutral hydrogen flow across the heliospheric interface. Science 307(5714), 1447–1449 (2005). https://doi.org/10.1126/science.1197340

Lallement R., E. Quémerais, D. Koutroumpa, J.L. Bertaux, S. Ferron, W. Schmidt, P. Lamy, The interstellar H flow: updated analysis of SOHO/SWAN data, in Twelfth International Solar Wind Conference, ed. by M. Maksimovic, K. Issautier, N. Meyer-Vernet, M. Moncuquet, F. Pantellini. American Institute of Physics Conference Series, vol. 1216 (2010), pp. 555–558. https://doi.org/10.1063/1.3395925.

Machol, J., Snow, M., Woodraska, D., Woods, T., Viereck, R., & Coddington, O. (2019), An improved lyman-alpha composite, Earth and Space Science, 6, 2263‐2272. https://doi.org/10.1029/ 2019EA000648

Matta, M. M. (2013), Modeling the Martian Ionosphere, PhD, Boston Univ., Boston, Mass.

Mayyasi, M., Clarke, J., Bhattacharyya, D., Deighan, J., Jain, S., Chaffin, M., ... Jakosky, B. (2017a). The variability of atmospheric deuterium brightness at Mars: Evidence for seasonal dependence. Journal of Geophysical Research: Space Physics, 122. https://doi.org/ 10.1002/2017JA024666.

Mayyasi, M., et al. (2017b), IUVS echelle-mode observations of interplanetary hydrogen: Standard for calibration and reference for cavity variations between Earth and Mars during MAVEN cruise, J. Geophys. Res. Space Physics, 122, doi:10.1002/ 2016JA023466.

Mayyasi, M., Withers, P., & Fallows, K. (2018). A sporadic topside layer in the ionosphere of Mars from analysis of MGS radio occultation data. Journal of Geophysical Research: Space Physics, 123, 883–900. https://doi.org/10.1002/ 2017JA024938

Mayyasi, M., Clarke, J., Bhattacharyya, D., Chaufray, J. Y., Benna, M., Mahaffy, P., et al. (2019a). Seasonal variability of deuterium in the upper atmosphere of Mars. Journal of Geophysical Research: Space Physics, 124, 2152–2164. https://doi. org/10.1029/2018JA026244.

Mayyasi, M., Narvaez, C., Benna, M., Elrod, M., & Mahaffy, P. (2019b). Ion - neutral coupling in the upper atmosphere of Mars: A dominant driver of topside ionospheric structure. Journal of Geophysical Research: Space Physics, 124. https://doi.org/10.1029/ 2019JA026481

Mayyasi, M. J. Clarke, J.-L. Bertaux, J. Deighan, D. Bhattacharyya, M. Chaffin, S. Jain, N. Schneider, S. Curry (2022a), Upgrades to the MAVEN Echelle Data Reduction Pipeline: New Calibration Standard and Improved Faint Emission Detection Algorithm at Lyman-□, Earth and Space Sciences, doi: 10.1029/2022EA002602.

Mayyasi, M., J. Clarke, J.-Y. Chaufray, D. Kass, S. Bougher, D. Bhattacharyya, J. Deighan, S. Jain, N. Schneider, G. L. Villanueva, F. Montmessin, M. Benna, P. Mahaffy, B. Jakosky

583 (2022b), Solar Cycle and Seasonal Variability of H in the Upper Atmosphere of Mars,
584 Icarus, https://doi.org/10.1016/j.icarus.2022.115293.
585
586 McClintock, W., et al. (2014), The Imaging Ultraviolet Spectrograph (IUVS) for the
587 MAVEN mission, Space Sci. Rev., doi:10.1007/s11214-014-0098-7.
588
589 Quémerais, E. (2000), Angle dependent partial frequency redistribution in the
590 interplanetary medium at Lyman α, Astron. Astrophys, 358, 353 – 367.
591
592 Quémerais, E., J.-L. Bertaux, R. Lallement, M. Berthé, E. Kyrölä, and W. Schmidt (1999),
593 Interplanetary Lyman α line profiles derived from SWAN/SOHO hydrogen cell
594 measurements: Full-sky Velocity Field, J. Geophys. Res., 104, A6, p 12,585 – 12,603,
595 1998JA900101.
596
597 Quémerais, E., R. Lallement, J.-L. Bertaux, D. Koutroumpa, J. Clarke, E. Kyrölä, and W.
598 Schmidt (2006), Interplanetary Lyman-α line profiles: Variations with solar activity cycle,
599 Astron. Astrophys., 445, 1135–1142, doi:10.1051/0004-6361:20065169.
600
601 Quémerais, E., B. McClintock, G. Holsclaw, O. Katushkina, and V. Izmodenov (2014),
602 Hydrogen atoms in the inner heliosphere: SWAN-SOHO and MASCS-MESSENGER
603 observations, J. Geophys. Res. Space Physics, 119, 8017–8029,
604 doi:10.1002/2014JA019761.
605
606 Thomas, G. and R. Krassa (1971), OGO 5 Measurements of the Lyman Alpha Sky
607 Background, Astron. & Astrophys., 11, p. 218.
608
609 Vincent, F. E., O. A. Katushkina, L. Ben-Jaffel, W. M. Harris, V. Izmodenov, E. Quémerais,
610 D. Koutroumpa, and J. Clarke (2014), Observations of the interplanetary hydrogen
611 during solar cycle 23 and 24. What can we deduce about the local interstellar medium?,
612 Astrophys. J. Lett., 788, L25.
613
614 Vincent, F., L. Ben-Jaffel, and W. Harris (2011), Updated analysis of the upwind
615 Interplanetary Hydrogen velocity as observed by the Hubble Space Telescope during
616 Solar Cycle 23, Astrophys. J., 738, 135, doi:10.1088/0004-637X/738/2/135.
617
618 Wu, F and D. Judge, A reanalysis of the observed interplanetary hydrogen Lα emission
619 profiles and the derived local interstellar gas temperature and velocity (1980), Ap. J.,
620 239. 389 – 394, 1980ApJ…239...389W.
621
622 Zank, G., V, Sterken, J. Giacalone, E. Möbius, R. von Steiger, E. Stone, S. Krimigis, J.
623 Richardson, J. Linsky, V. Izmodenov, B. Heber (2022), The Early History of Heliospheric
624 Science and the Spacecraft That Made It Possible, Space Science Reviews, 218:34
625 https://doi.org/10.1007/s11214-022-00900-8.